Journal of Quantitative Spectroscopy & Radiative Transfer 170 (2016) 54–68

Contents lists available at ScienceDirect

Journal of Quantitative Spectroscopy & Radiative Transfer

journal homepage: www.elsevier.com/locate/jqsrt

Influence of 3D effects on 1D aerosol retrievals in synthetic, partially clouded scenes

F.A. Stap [a,b,*], O.P. Hasekamp [a], C. Emde [c], T. Röckmann [b]

[a] SRON Netherlands Institute for Space Research, Sorbonnelaan 2, 3584 CA Utrecht, The Netherlands
[b] Institute for Marine and Atmospheric Research (IMAU), Utrecht University, Princetonplein 5, 3584 CC Utrecht, The Netherlands
[c] Meteorological Institute, Ludwig-Maximilians-University, Theresienstr. 37, D-80333 Munich, Germany

ARTICLE INFO

Article history:
Received 21 July 2015
Received in revised form
15 October 2015
Accepted 15 October 2015
Available online 11 November 2015

Keywords:
Aerosol
Clouds
3D effects
Remote sensing

ABSTRACT

An important challenge in aerosol remote sensing is to retrieve aerosol properties in the vicinity of clouds and in cloud contaminated scenes. Satellite based multi-wavelength, multi-angular, photo-polarimetric instruments are particularly suited for this task as they have the ability to separate scattering by aerosol and cloud particles. Simultaneous aerosol/cloud retrievals using 1D radiative transfer codes cannot account for 3D effects such as shadows, cloud induced enhancements and darkening of cloud edges. In this study we investigate what errors are introduced on the retrieved optical and micro-physical aerosol properties, when these 3D effects are neglected in retrievals where the partial cloud cover is modeled using the Independent Pixel Approximation. To this end a generic, synthetic data set of PARASOL like observations for 3D scenes with partial, liquid water cloud cover is created. It is found that in scenes with random cloud distributions (i.e. broken cloud fields) and either low cloud optical thickness or low cloud fraction, the inversion algorithm can fit the observations and retrieve optical and micro-physical aerosol properties with sufficient accuracy. In scenes with non-random cloud distributions (e.g. at the edge of a cloud field) the inversion algorithm can fit the observations, however, here the retrieved real part of the refractive indices of both modes is biased.

1. Introduction

Aerosol affects the radiative forcing of the Earth's atmosphere directly by scattering and absorbing radiation and indirectly by acting as cloud condensation nuclei. The current understanding of the radiative forcing due to aerosol radiation interactions and aerosol cloud interactions is limited, as assessed by the latest IPCC report [1]. Here, the uncertainty on the aerosol radiative forcing is the largest contribution to the uncertainty on the total radiative forcing. Improving measurement based estimates of the radiative forcing by aerosols requires long-term, global monitoring of aerosol and cloud properties. In particular, it requires observations of the aerosol micro-physical and optical properties, such as the complex refractive index, the size distribution, the number of particles, the Single Scattering Albedo (SSA), and the Aerosol Optical Thickness (AOT).

The optical and micro-physical aerosol parameters mentioned above can only be unambiguously retrieved from observations by multi-angle, photo-polarimeters. This has been demonstrated by theoretical studies [2–6] as well as by case studies using airborne measurements [7–9] and studies using the POLDER-3 instrument on board the PARASOL satellite [10–12].

These studies are restricted to observations of scenes that are either cloud free or have an aerosol layer lifted above a homogeneous cloud layer. The separation of cloudy and cloud-free observations requires an adequate

* Corresponding author.
E-mail address: arjenstap@gmail.com (F.A. Stap).

http://dx.doi.org/10.1016/j.jqsrt.2015.10.008
0022-4073/

cloud screening, which, if not applied strict enough can cause large errors in the retrieved aerosol properties. The down-side of performing a strict cloud screening is not only the obvious data loss, but especially the systematic removal of near cloud scenes. This is unfortunate as, in the transitional zone between clouds and cloud-free sky, increased scattering is expected due to hydrated aerosol and undetected cloud particles [13–15]. Note that 3D effects and detector blurring also contribute to the increased reflectances in these zones [16,17].

Stap et al. [18] used characteristic features of cloud scattering in multi-angle photo-polarimetric PARASOL measurements to perform cloud screening based on a goodness-of-fit criterion for aerosol retrievals. The next step would be to retrieve aerosol properties in near cloud and partially clouded scenes. This would allow for a more complete and more representative knowledge of the global aerosol distribution. This requires retrieval algorithms that can deal with clouds and aerosol simultaneously. In a study on a synthetic data set [19] has shown the ability to separate aerosol from (liquid) cloud particles in multi-wavelength, multi-angular, photo-polarimetric observations, making use of distinctive angular features of cloud droplets scattering, such as the cloud bow. Waquet et al. [20,12] demonstrated the ability to separate aerosol and clouds when the aerosol is lofted above a homogeneous (liquid water) cloud field.

The study of [19] is based on 1 dimensional (1D) radiative transfer calculations taking into account partial cloudiness using the Independent Pixel Approximation (IPA). Due to the large computational cost of this type of retrievals, using 1D radiative transfer is presently the only feasible method for large scale (multi-year global) processing of photo-polarimetric measurements. It is however known that 3 dimensional (3D) radiative transfer effects may be significant in the neighborhood of clouds, e.g. due to shadows, side illumination, and 'bluing' [21,22]. Thus, it is important to investigate the fidelity of aerosol retrievals in partially cloudy scenes, as proposed by [19], in the presence of 3D radiative transfer effects. More specifically, it is important to find out for what situations (e.g. in terms of cloud cover, cloud optical thickness, and spatial distribution) simultaneous aerosol/cloud retrievals can still be performed with a 1D radiative transfer model and for which situations 3D radiative effects hamper a meaningful retrieval of aerosol properties.

The aim of the present paper is to present a generic, synthetic data set of PARASOL like observations for partially cloudy scenes using a 3D radiative transfer model. We will investigate in what situations the 3D synthetic measurements can be reproduced by a 1D forward model and whether in these cases the aerosol properties retrieved by a 1D algorithm for simultaneous aerosol/cloud retrieval are still sufficiently close to the aerosol properties used to calculate the synthetic measurements.

The retrieval algorithm for simultaneous aerosol/cloud retrievals from multi-angle photo-polarimetric measurements and the 3D radiative transfer code used to create the synthetic measurements are described in Section 2. In Section 3 the data set of 3D scenes of partial, liquid water cloud cover is presented. The difference between 1D and 3D radiative transfer calculations and the ability of the algorithm to retrieve the correct micro-physical and optical aerosol properties, while neglecting 3D effects, is discussed in Section 4. In Section 5 the results are summarized.

2. Methods

This section describes the 1D algorithm for the simultaneous retrieval of aerosol and cloud properties and the 3D radiative transfer model used to create synthetic multi-wavelength, multi-viewing-angle measurements of intensity and polarization.

2.1. Retrieval algorithm

2.1.1. Inversion

This study builds on the retrieval algorithm described in detail by [11], for aerosol retrieval in cloud free scenes from multi-angle photo-polarimetric measurements from the POLDER-3 instrument, onboard PARASOL. Here, we extend the algorithm to also retrieve cloud properties, simultaneously with aerosol properties, with the goal to perform aerosol retrievals in partially cloudy scenes.

In any retrieval method, the aim is to invert a forward model $\mathbf{F}$ that relates a state vector $\mathbf{x}$ with unknown fit parameters to a measurement vector $\mathbf{y}$, viz.

$$\mathbf{y} = \mathbf{F}(\mathbf{x}) + \mathbf{e}_y, \tag{1}$$

where $\mathbf{e}$ is an error term. The vector $\mathbf{y}$ contains the measurements of intensity and DoLP at different wavelengths and different viewing angles. The state vector $\mathbf{x}$ contains the aerosol parameters describing a bi-modal log-normal aerosol size distribution. For both the fine and the coarse mode the state vector includes the effective radius r_{eff}, the effective variance v_{eff} (see [23]), the real and the imaginary part of the refractive index $m = m_r + m_i$, and the column integrated aerosol number concentration N. Aerosols are assumed to be homogeneously distributed over the lowest 1.5 km of the atmosphere. In addition to the aerosol parameters, the state vector also includes the Cloud Optical Thickness (COT) and the Cloud Fraction (f) as fit parameters. The other cloud parameters (size distribution, top height, geometrical thickness) are assumed a priori. A black surface is being used for all simulations in this paper.

For the inversion, we use the Phillips–Tikhonov regularization method which finds the retrieved state vector $\hat{x}$ by minimizing a cost function that is the sum of the least squares cost function and a side constraint weighted by the regularization parameter γ ($\gamma \geq 0$) according to

$$\hat{\mathbf{x}} = \min_{\mathbf{x}} \left(||\mathbf{S}_{\mathbf{y}}^{-1/2}(\mathbf{F}(\mathbf{x}) - \mathbf{y})||^2 + \gamma ||\mathbf{W}(\mathbf{x} - \mathbf{x}_\alpha)||^2 \right) \tag{2}$$

At every iteration a regularization parameter is chosen by heuristically trying a range of values. Measurements are simulated for the state vectors resulting from the different regularization parameters using an approximate, but fast forward model (see Section 2.1.2). Afterwards the value of γ which best fits the measurement is chosen.

Since the forward model $\mathbf{F}(\mathbf{x})$ is generally nonlinear in $\mathbf{x}$, the inverse problem to estimate $\mathbf{x}$ from Eq. (1) is solved

iteratively by replacing $\mathbf{F}(\mathbf{x})$ through its linear approximation

$$\mathbf{F}(\mathbf{x}_{n+1}) \approx \mathbf{F}(\mathbf{x}_n) + \mathbf{K}(\mathbf{x}_{n+1} - \mathbf{x}_n), \tag{3}$$

with subscript n indicating the n-th iteration and $\mathbf{K}$ being the Jacobian matrix

$$K_{ij} = \frac{\partial F_i}{\partial x_j}(\mathbf{x_n}). \tag{4}$$

The iterative process is stopped when the difference in goodness-of-fit χ^2 is less than a certain threshold. The retrieval is considered successful if the final $\chi^2 < 2.0$. Here, the χ^2 threshold has empirically been determined appropriate.

In its standard setup, the first guess state vector is obtained using a lookup table based retrieval or alternatively, by a neural network retrieval (as in the work by [24]). In the present study however we want to focus on 3D effects and want to avoid cases where the retrieval does not converge because the first guess deviates too much from the truth. Therefore, for the synthetic retrievals of this paper we use the truth as first guess.

2.1.2. Forward model

The forward model $\mathbf{F}$ for a partially cloudy scenes is based on the independent pixel approximation:

$$\mathbf{F} = (1-f)\mathbf{F}_{\text{clear}} + f\mathbf{F}_{\text{cloud}}, \tag{5}$$

where $\mathbf{F}_{\text{clear}}$ and $\mathbf{F}_{\text{cloud}}$ are the forward models for a cloud free and fully cloudy atmosphere, respectively, and f is the cloud fraction.

Both $\mathbf{F}_{\text{clear}}$ and $\mathbf{F}_{\text{cloud}}$ contain two main parts. The first part calculates optical properties (scattering and absorption optical thickness, scattering phase matrix) from the micro-physical aerosol and cloud properties. For this part of the forward model, pre-calculated optical properties as a function of the size parameters and of the real and the imaginary part of the refractive index [25] are being used. The optical properties are pre-calculated for spheres and spheroids with an axis ratio distribution as proposed by [25]. Aerosols are described by mixture of spheres and spheroids where optical properties for a given refractive index are obtained by spline interpolation from the tabulated values. Cloud droplets are described by spheres with the wavelength dependent refractive index of water [26]. Finally, the aerosol and cloud optical properties are combined with Rayleigh scattering optical properties. Molecular absorption is neglected in this study. The model atmosphere is vertically discretized in 36 homogeneous layers between 0 and 40 km.

The second part of $\mathbf{F}_{\text{clear}}$ and $\mathbf{F}_{\text{cloud}}$ solves the vector radiative transfer equation for a plane parallel horizontally homogeneous atmosphere for the given optical properties in different altitude layers in the atmosphere. For this part we employ the Gauss–Seidel radiative transfer model developed at SRON Netherlands Institute for Space Research [27–29], hereafter referred to as the SRON-GS model. The SRON-GS model calculates the Jacobian matrix $\mathbf{K}$ in an analytical way by employing the forward-adjoint perturbation theory for vector radiative transfer [27–29]. Unless otherwise stated, we discretize the diffuse radiation field in 16 Gaussian streams for the forward model calculations in this paper. To handle strongly peaked phase functions with this limited number of streams we use the multiple-scattering correction of [30].

2.2. The MYSTIC 3D radiative transfer code

The multi-wavelength, multi-viewing-angle synthetic measurements of intensity and Degree of Linear Polarization (DoLP) used in this study are created by the 3D radiative transfer model MYSTIC (Monte Carlo for the physically correct tracing of photons in cloudy atmospheres) [31–33]. MYSTIC is one of the solvers of the radiative transfer equations in libRadtran [34]. It traces a given number of photons as they enter the scene, either at the top of the atmosphere or at the surface, and traces them until they are absorbed or leave the scene. Several methods are applied to optimize the algorithm; (i) the 'local estimate method' [35] which, at each scattering point, takes into account the probability that the photon is scattered towards the sun/detector, and (ii) the 'variance reduction optimal options method' [36] which reduces the noise that arises when dealing with spiky phase functions while using the local estimate method.

The statistical nature of the Monte Carlo method leads to the so-called photon noise on the result. An appropriate amount of photons is used in each calculation to ensure that the photon noise in each synthetic measurement is well below 1% on the intensity and 0.005 (absolute on the DoLP). The boundaries of the 3D model are periodic, meaning that a photon leaving the scene on the western boundary will re-enter at the eastern boundary. The scenes are divided in a sufficient number of sample grid cells. The synthetic measurement is obtained by averaging the radiances of the observed sample grid cells.

All models have a black surface, thus the synthetic measurements can be interpreted as an approximation of over ocean observations. The scattering and absorption properties of the atmosphere (including air molecules, clouds, and aerosols) as a function of altitude and wavelength are provided to the MYSTIC model via an input file specifying 36 vertical layers between 0.0 and 40.0 km. The molecular, aerosol and cloud optical properties are calculated in the same way as in the retrieval algorithm so that we do not introduce differences with the 1D model used in the retrieval other than those caused by 3D effects.

3. Synthetic 3D data set

A large set of generic synthetic measurements for different 3D atmospheres has been created that contains the various 3D effects that are important for the retrieval of aerosol properties. The measurements are representative for the POLDER-3 instrument onboard the PARASOL satellite. Radiances are simulated for the 490, 670, 865 and 1020 nm bands, where the intensity and polarization are considered for the first three of those and only intensity is used for the latter band. Two ground pixel sizes are explored, which represent the PARASOL Full Resolution (FR) and Medium Resolution (MR) ground pixels of, respectively 6.2×6.2 km and 18.6×18.6 km.

Table 1
For the 10 aerosol cases used in this study, the randomly selected AOT of each mode ($\tau_{550\ \mathrm{nm}}$), where superscripts f and c indicate fine or coarse mode, followed by the effective radius (r_{eff}), effective variance (v_{eff}), the real and the imaginary part of the complex refractive index (m_{r} and m_{i}), and (for the coarse mode only) a fraction of spherical particles (*Sph*).

ID	$\tau^{\mathrm{f}}_{550\ \mathrm{nm}}$	$\tau^{\mathrm{c}}_{550\ \mathrm{nm}}$	$r^{\mathrm{f}}_{\mathrm{eff}}$	$v^{\mathrm{f}}_{\mathrm{eff}}$	$m^{\mathrm{f}}_{\mathrm{r}}$	$m^{\mathrm{f}}_{\mathrm{i}}$	$r^{\mathrm{c}}_{\mathrm{eff}}$	$v^{\mathrm{c}}_{\mathrm{eff}}$	$m^{\mathrm{c}}_{\mathrm{r}}$	$m^{\mathrm{c}}_{\mathrm{i}}$	Sph^{c}
1	0.21	0.31	0.46	0.12	1.50	1.5E−05	1.83	0.16	1.64	2.6E−02	0.76
2	0.19	0.30	0.39	0.13	1.51	1.7E−01	1.22	0.28	1.59	2.2E−03	0.64
3	0.08	0.08	0.24	0.18	1.56	1.1E−05	1.13	0.39	1.61	1.6E−02	0.14
4	0.15	0.34	0.10	0.68	1.40	4.2E−03	0.90	0.49	1.41	1.9E−02	0.11
5	0.30	0.31	0.12	0.30	1.46	2.2E−01	1.71	0.31	1.37	1.8E−04	0.04
6	0.25	0.14	0.05	0.52	1.44	5.4E−02	2.95	0.64	1.59	3.3E−04	0.22
7	0.13	0.32	0.27	0.24	1.62	1.2E−04	1.37	0.28	1.38	1.3E−03	0.50
8	0.25	0.26	0.06	0.40	1.49	1.2E−03	2.47	0.64	1.62	6.7E−04	0.11
9	0.17	0.28	0.23	0.54	1.42	1.0E−01	1.92	0.36	1.60	3.7E−02	0.11
10	0.19	0.13	0.22	0.65	1.58	3.5E−05	1.42	0.12	1.42	4.7E−05	0.08

For all simulations aerosols are homogeneously distributed between 0.0 and 1.5 km altitude in the atmosphere. The aerosol parameters used for the creation of synthetic measurements are listed in Table 1. They are randomly chosen between realistic boundaries. Note that the aerosol distribution has plane-parallel symmetry and thus produces no 3D effects itself.

Two essentially different horizontal distributions of liquid water clouds are explored; a random distribution of cuboid clouds to simulate broken cloud fields, which is described in Section 3.1 and a large continuous slab of cloud near the edge of the scene of interest, which is described in Section 3.2. All clouds have a gamma size-distribution with a fixed effective radius of 12.0 μm and a fixed effective width of 0.1 μm. Three cloud optical thicknesses (COT) are explored ($\tau^{\mathrm{cloud}}_{550\ \mathrm{nm}} = 1.0$, 5.0, and 10.0) for a variety of different vertical distributions.

The clouds simulated in this study are simplifications of real clouds; they are cuboids with smooth surfaces and micro-physical properties that remain constant throughout the cloud. Nevertheless, these simple clouds are sufficient to model important 3D effects like shadows, illumination of the cloud free column and illumination of the sides of the clouds. We have chosen this simple cloud representation over for example a Large Eddy Simulation (LES), because it allows us to systematically investigate the influence of the cloud fraction, COT and cloud height, while still containing the most important 3D effects mentioned above.

Six different solar and satellite geometries are investigated. These are summarized in Table 2 and described by the solar zenith angle (θ_{sun}), the solar azimuth angle (ϕ_{sun} measured clockwise with respect to the South) and the satellite azimuth angle (ϕ_{sat} measured clockwise with respect to the North). Note that the absolute, relative azimuth angle ($\phi = \phi_{\mathrm{sun}} - \phi_{\mathrm{sat}}$) is identical for all six geometries. We note that 1D RT models are dependent on the absolute, relative azimuth angle rather than ϕ_{sun} and ϕ_{sat} separately. Thus, in 1D there is no distinction between the models with geometries *i–iii* or models with geometries *iv–vi* in Table 2. The differences in the models with geometries *i–iii* (or *iv-vi*) give an indication of the variation due to the 3D viewing geometry that cannot be captured with 1D RT codes.

3.1. Broken cloud fields

Broken cloud fields are simulated for small and medium sized clouds of, respectively, 100×100 m and 516×516 m horizontally with aspect ratios (defined as vertical versus horizontal length) of 1 and 2. The clouds are randomly distributed over a horizontal grid with cells of the same size as the clouds, i.e. there are no overlapping clouds. An example of the intensity distribution for a broken cloud scene is given in Fig. 1. Synthetic measurements are created for three COTs ($\tau^{\mathrm{cloud}}_{550\ \mathrm{nm}} = 1.0$, 5.0 and 10), six cloud fractions (f=0.02, 0.05, 0.10, 0.15, 0.20 and 0.25) and four vertical cloud profiles (1.5–1.6, 1.5–1.7, 2.0–2.1 and 2.5–2.6 km).

Two ground pixel sizes are explored; the PARASOL FR and MR ground pixels of respectively 6.2×6.2 km and 18.6×18.6 km. The spatial dimensions of the 3D models are equal to the ground pixel sizes. Thus, these models are representative for observations of a broken cloud field, which has constant parameters over an area larger than the ground pixel size.

3.2. Cloud edge cases

The 'edge' scenarios simulate retrievals near the edge of a large, continuous cloud field for both the FR and MR PARASOL observations. In these scenarios the cloud is situated in the Western region. Thus, for $\phi_{\mathrm{sun}} = 20^{\circ}$ a shadow is cast in the clear part of the scene and for $\phi_{\mathrm{sun}} = 320^{\circ}$ the Eastern side of the cloud is illuminated.

For such cloud distributions the viewing angle is of particular importance; at certain viewing angles the cloud may obscure the cloud-free part of the scene ($f > f_{\mathrm{nadir}}$, where f_{nadir} is the cloud fraction at nadir), while at other viewing angles a part of the atmosphere beneath the cloud is observed ($f < f_{\mathrm{nadir}}$). In order to model these differences in the observed columns at the various viewing zenith angles, the spatial dimensions of the 'edge' scenarios are larger than the ground pixel size of PARASOL. Due to the symmetry in latitudinal direction of the scene there is only need to increase the size of the scene in longitudinal direction. The synthetic, FR measurements are obtained from scenes that are 6×1 FR PARASOL pixels large in longitudinal versus latitudinal direction (37.2×6.2 km). The synthetic, MR measurements are obtained from scenes that are 8×3 FR

Table 2
A summary of the six solar and satellite geometries that are explored. Note that the satellite moves from the first stated azimuth angle through zenith to the second stated azimuth angle.

Geometry	θ_{sun}	ϕ_{sun}	ϕ_{sat}
i	40°	20°	0° to 180°
ii	40°	0°	−20° to 160°
iii	40°	320°	−20° to 160°
iv	60°	20°	0° to 180°
v	60°	0°	−20° to 160°
vi	60°	320°	−20° to 160°

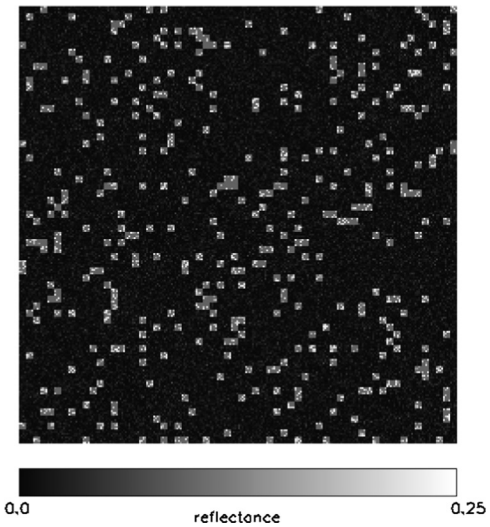

Fig. 1. A scene with a broken cloud field viewed from nadir at 670 nm. The scene has 10% cloud cover between 1.5 and 1.6 km, with $\tau^{cloud}_{550\ nm} = 5.0$.

PARASOL pixels large in longitudinal versus latitudinal direction (49.6 × 18.6 km). In both the FR and MR simulations only the three most Western FR PARASOL pixels are covered by the cloud. This setup ensures that the horizontal distance between the Eastern border of the observed column and the Eastern border of the scene (and thus Western edge of the cloud) is at least 10 km at all viewing angles. At this distance of the cloud we assume the contribution due to 3D radiative effects to be negligible.

The synthetic measurements are created for six cloud fractions (f=0.02, 0.05, 0.10, 0.15, 0.20 and 0.25), with models of three different COTs ($\tau^{cloud}_{550\ nm} = 1.0$, 5.0 and 10), and five vertical cloud profiles (1.5–1.6, 1.5–2.0, 1.5–2.5, 2.0–2.1 and 2.5–2.6 km). Fig. 2 shows a nadir image of a MR PARASOL ground pixel as an example.

4. Results

In this section we first compare the MYSTIC and SRON-GS radiative transfer codes for 1D scenes in order to check consistency. Next we study 3D effects on intensity and DoLP by comparing MYSTIC 3D calculations with SRON-GS calculations using the independent pixel approximation. Finally, we investigate errors on retrieved aerosol properties in partially cloudy scenes for retrievals based on the independent pixel approximation. To this end, we apply our algorithm for simultaneous aerosol/cloud retrieval as described in Section 2.1 to synthetic measurements created with the MYSTIC model for the 3D scenes described in Section 3.

4.1. Comparison of intensity and DoLP

4.1.1. Comparison for 1D scenes

In order to check the agreement between the SRON-GS and the MYSTIC model for 1D scenes, Figs. 3–5 show a comparison of the SRON-GS and MYSTIC codes for three cases: (i) Rayleigh atmosphere, (ii) Rayleigh + aerosol, (iii) Rayleigh and an aerosol layer below a thin ($\tau^{cloud}_{550\ nm} = 5.0$), liquid water cloud. The standard deviation between the SRON-GS and MYSTIC models in cases (i) and (ii) is roughly 0.3% on the intensity and below 0.001 (absolute) on the DoLP. These differences are due to the photon noise of the Monte Carlo simulations. For the cloud case, differences are somewhat larger, especially near the cloud-bow and backscattering angle. The reason for this is that the SRON-GS model uses a discretization of the radiation field in 16 streams which causes errors for the highly peaked phase functions of cloud droplets. When (at considerable computational cost) 64 streams are used in the SRON-GS code, the standard deviation of the two models is below 0.4% on I and 0.001 (absolute) on DoLP. The errors due to the use of 16 streams will however be significantly smaller for partially cloudy scenes with small cloud fraction ($\leq 25\%$). For those scenes the 3D induced errors are dominant. Since we focus our study on those partially cloudy scenes, we perform our retrievals using 16 streams in the SRON-GS model, avoiding unfeasible computation times.

4.1.2. Comparison for 3D scenes

Fig. 6 gives an example of the differences between a 3D and 1D simulation for a broken cloud field for geometries *i* through *iii* (see Table 2). For this example with $\tau^{cloud}_{550\ nm} = 5.0$ and f=0.05, the systematic differences range up to 20% in intensity and 0.06 (absolute) on DoLP depending on the wavelength and scattering angle. For higher cloud fractions and higher COT these differences become even larger.

The variation in the (horizontal) cloud size, the solar and satellite azimuth angles and the ground pixel size results in twelve different 3D simulations with only one 1D counterpart. Fig. 6 already gives an example of the range in 3D models due to different solar and satellite azimuth angles, which cannot be captured with the 1D model. Varying the solar azimuth angle changes the shadow fraction in the scene as well as the illumination of the sides of the clouds. At off nadir viewing angles, varying the satellite azimuth angle changes the observed cloud fraction, since the projection of the surfaces of the clouds onto the detector change. These differences, for this example, range from 0–2% in intensity and 0–0.005 in DoLP and are systematic. Varying the ground pixel size does not affect the radiances observed in the 3D scene if the cloud distribution is close enough to a random distribution. Differences in the cloud size change the relative volume of sky that is near a cloud, where cloud induced enhanced reflectances are expected to be stronger. However,

the differences between models with small clouds at both ground pixel sizes and the models with medium sized clouds at the MR ground pixel size are random and relatively small, namely in the order of a few percent on the intensity and less than 0.005 in DoLP (not shown). Therefore, we limit the analysis in the remainder of this paper to one cloud size; the small clouds, and one ground pixel size; the FR PARASOL pixels.

In order to efficiently summarize the difference between 1D simulations using the independent pixel approximation and 3D MYSTIC calculations for broken cloud fields with randomly distributed clouds for multi-angle photo-polarimetric measurements, Fig. 7 shows the χ^2 between the 3D and 1D simulations for different COT, cloud fraction and aspect ratio of the clouds. Here, the χ^2 difference is calculated assuming a measurement uncertainty of 1% on the intensity and 0.005 (absolute) on the DoLP, representative for PARASOL measurements over the ocean.

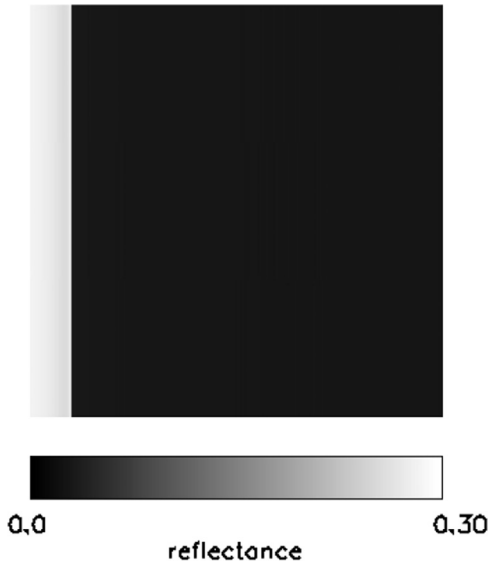

Fig. 2. Nadir image of an 'edge' case at 670 nm for the model with a cloud of optical thickness $\tau^{\text{cloud}}_{550\text{ nm}} = 5.0$, between 1.5 and 2.5 km. The image shows a MR PARASOL ground pixel with a cloud fraction of 10%. The sun is situated in the South-East ($\phi_{\text{sun}} = 320^\circ$, $\theta_{\text{sun}} = 40^\circ$) and illuminates the Eastern side of the cloud.

The range in the polygons of Fig. 7 corresponds to mostly to different values of the aerosol load, solar zenith and azimuth angle. The influence on this range due to the three explored cloud heights and the different satellite azimuth angles is very small. The 3D effects are very small for models with small cloud fraction of optically thin clouds. Note, however, that the differences here are systematic rather than random. At aspect ratio 2 the contribution to the observed cloud fraction by the sides of the cloud is larger. This leads to larger differences with the 1D models at the higher viewing zenith angles. Furthermore, the larger area of the cloud sides for aspect ratio 2 also causes larger shadows and also larger cloud induced radiance enhancements in the cloud free columns. At higher COTs, light is more efficiently reflected by the cloud, leading to stronger cloud induced enhancements. Altogether this results in larger χ^2 differences between the 1D and 3D models at higher aspect ratios and larger COTs.

Fig. 8 shows a comparison of 3D models for an 'edge' cloud scene at three different viewing geometries and their 1D counterpart. For the 'edge' cases, the geometry causes larger differences between the 3D models than is the case for the broken cloud fields. The 3D model with geometry *i* shows relatively small differences with the 1D model. Here, the satellite moves from $\phi_{\text{sat}} = 0^\circ$ to $\phi_{\text{sat}} = 180^\circ$ through zenith. Thus, the side of the cloud is not observed and the cloud fraction is identical at all

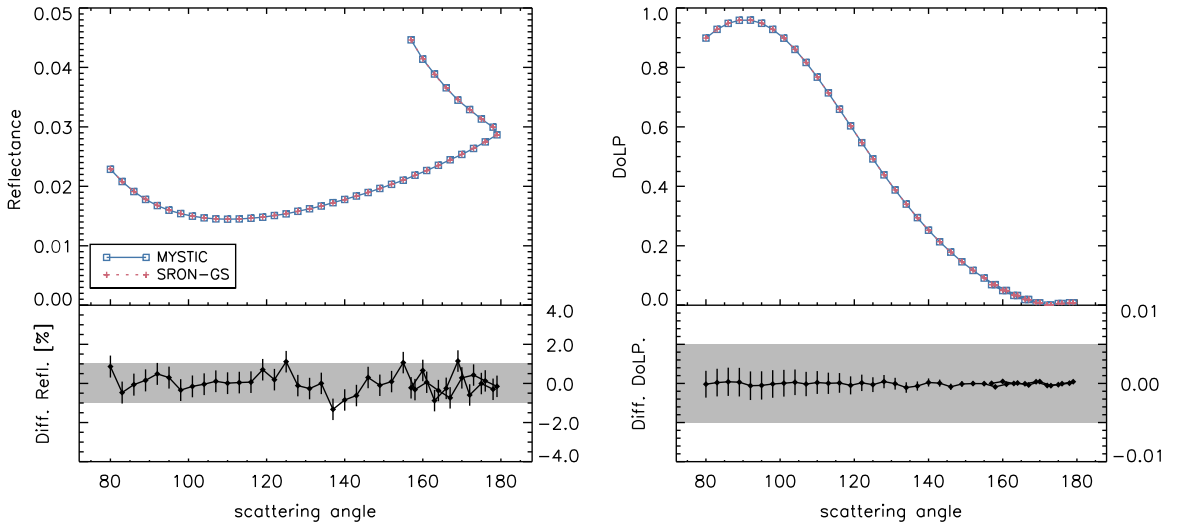

Fig. 3. The comparison of the SRON-GS and MYSTIC radiative transfer codes for the Rayleigh case. The top left and right panels show the reflectance and DoLP at 670 nm. The bottom panels show the relative difference in reflectance and absolute difference in DoLP. Here the gray bar indicates the measurement uncertainty and the black vertical bars show the photon noise of the Monte Carlo simulation. Note that the scattering angle range from 157° to 179° is observed twice, but that these observations are at different viewing angles. The observed radiances have therefore traveled different paths through the atmosphere.

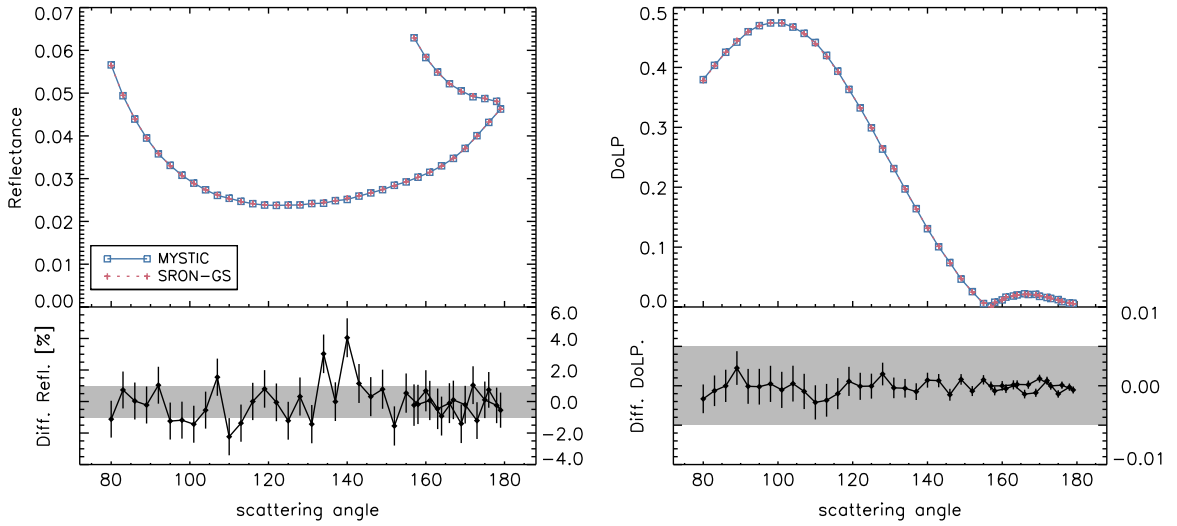

Fig. 4. The same as Fig. 3, but for the aerosol case. The aerosol is homogeneously distributed between 0.0 and 1.5 km.

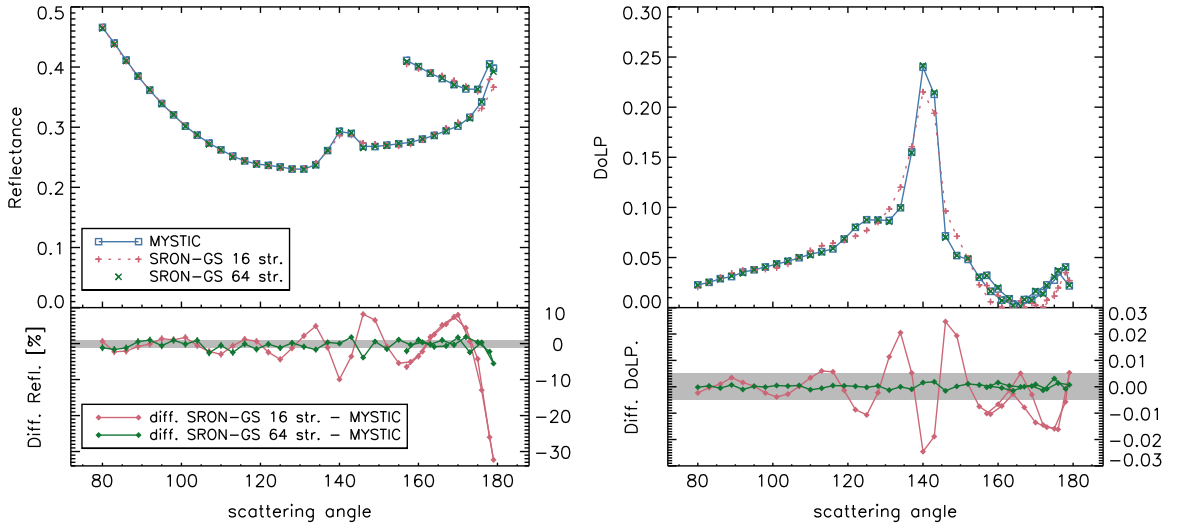

Fig. 5. The same as Fig. 3, but for the aerosol below cloud case. The aerosol is homogeneously distributed between 0.0 and 1.5 km and the liquid water cloud, with $\tau_{550\,\mathrm{nm}}^{\mathrm{cloud}} = 5.0$, is homogeneously distributed between 1.5 and 1.6 km.

viewing angles. For this geometry the sun is situated in the South-West and therefore the cloud casts a shadow in the cloud-free part of the scene. For geometries *i* and *iv* the important 3D effects are the shadow, cloud induced enhancements and darkening of the cloud near the edge. Compared to the models with the other geometries, which are discussed below, the 3D effects in models with these geometries are modest.

When the satellite moves from $\phi_{\mathrm{sat}} = -20^{\circ}$ to $\phi_{\mathrm{sat}} = 160^{\circ}$ through zenith more 3D effects come into play (see for example models 3D*ii* and 3D*iii* in Fig. 8). Here, the side of the cloud is observed and, more importantly, the observed cloud fraction differs between viewing angles. At scattering angles lower than 140° (120° for geometry *v* and *vi*), since the cloud obscures part of the cloud free column, a larger cloud fraction and thus higher reflectance is observed. The opposite is true for scattering angles higher than 140°. This inhomogeneity of the scene at the different viewing angles is the main cause for differences with the 1D model simulations in geometries *ii*, *iii*, *v* and *vi*

In geometries *ii* and *v* the sun is situated in the south, therefore the shadow is restricted to the cloudy column, and is only observed at those viewing angles that can observe the atmosphere below the cloud. Compared to the synthetic measurements of geometries *i* and *vi*, these geometries have smaller 3D effects due to the shadow and larger 3D effects due to the inhomogeneity at different viewing angles.

For geometries *iii* and *vi* the sun is situated in the South-East. Therefore the side of the cloud is illuminated, increasing the cloud induced enhancements in the cloud free column. Furthermore, part of the atmosphere below the cloud is directly illuminated by the sun. The main difference in the synthetic measurements of geometries *ii*

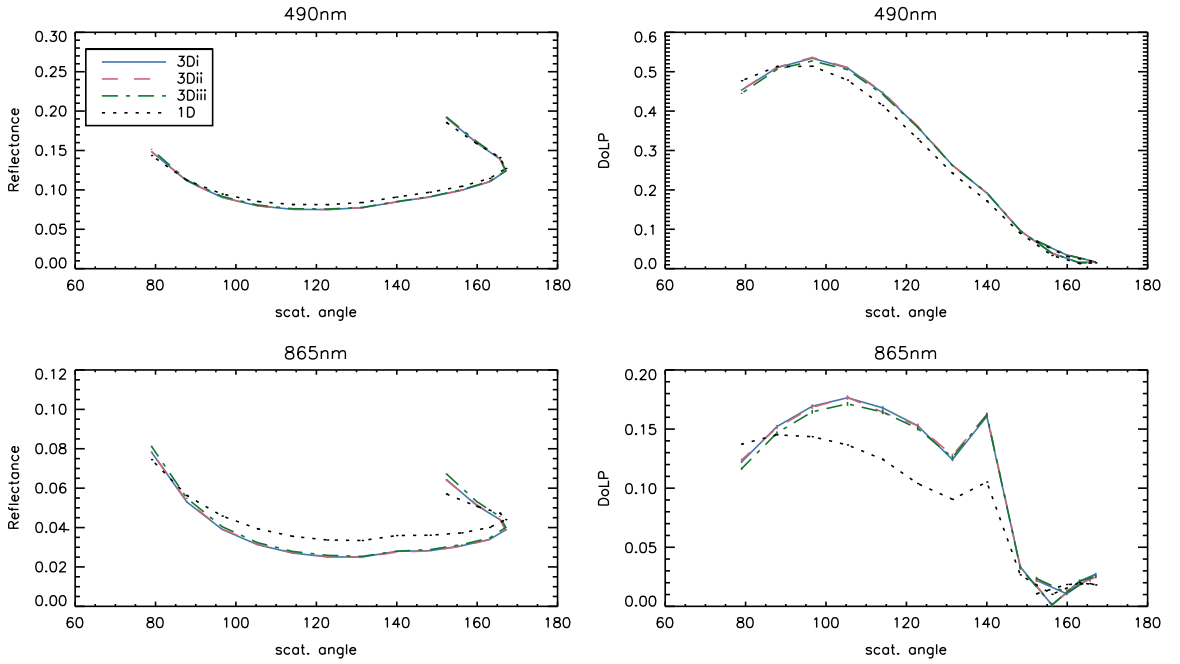

Fig. 6. Comparison of 3D broken cloud field models with geometries *i–iii* (see Table 2) and their 1D counterpart. The scene has the size of a FR PARASOL ground pixel. There is 5% cloud cover consisting of small clouds, with $\tau_{550\ \mathrm{nm}}^{\mathrm{cloud}} = 5.0$, between 1.5 and 1.6 km.

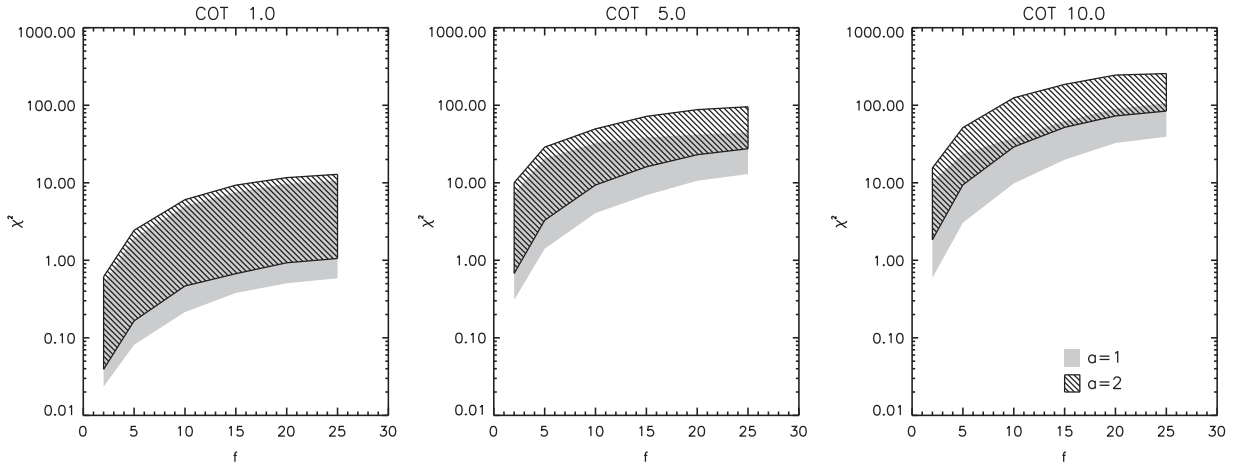

Fig. 7. Quantification of the 3D effects in terms of χ^2 for the broken cloud field models, as a function of cloud fraction (f). The models are separated on COT and aspect ratio (a). Each polygon shows the range in χ^2 which is mostly determined by the aerosol load as well as the solar zenith and azimuth angles. Differences due the three explored cloud heights and the different satellite azimuth angles are negligible.

and *v* versus those of geometries *iii* and *vi* originates from the side illumination of the cloud.

Especially the inhomogeneity at the different viewing angles is a 3D aspect that causes large differences with the 1D forward model. This is in part due to the fact that the 1D forward model is intrinsically homogeneous at all viewing angles.

In Fig. 9 the 3D effects in the edge cloud models (with a vertical cloud profile between 1.5 and 1.6 km) are quantified in terms of χ^2, similar to Fig. 7. The differences due to 3D effects are mostly influenced by the COT, viewing geometry, solar azimuth angle and to a lesser degree, by the aerosol load and solar zenith angle. Similar figures are found for the other cloud heights and geometrical thicknesses.

For the fortunate viewing geometries (*i* and *iv*), the shadow and cloud induced enhancements cause relatively small, but systematic differences with the 1D simulations. These two 3D effects have an opposite impact on the synthetic measurements; the shadow reduces the aerosol and Rayleigh signal in cloud free column, while the cloud induced enhancements increase this signal. These competing effects generally reduce the net difference with the 1D models best for the models with geometry *iv* (SZA=60°).

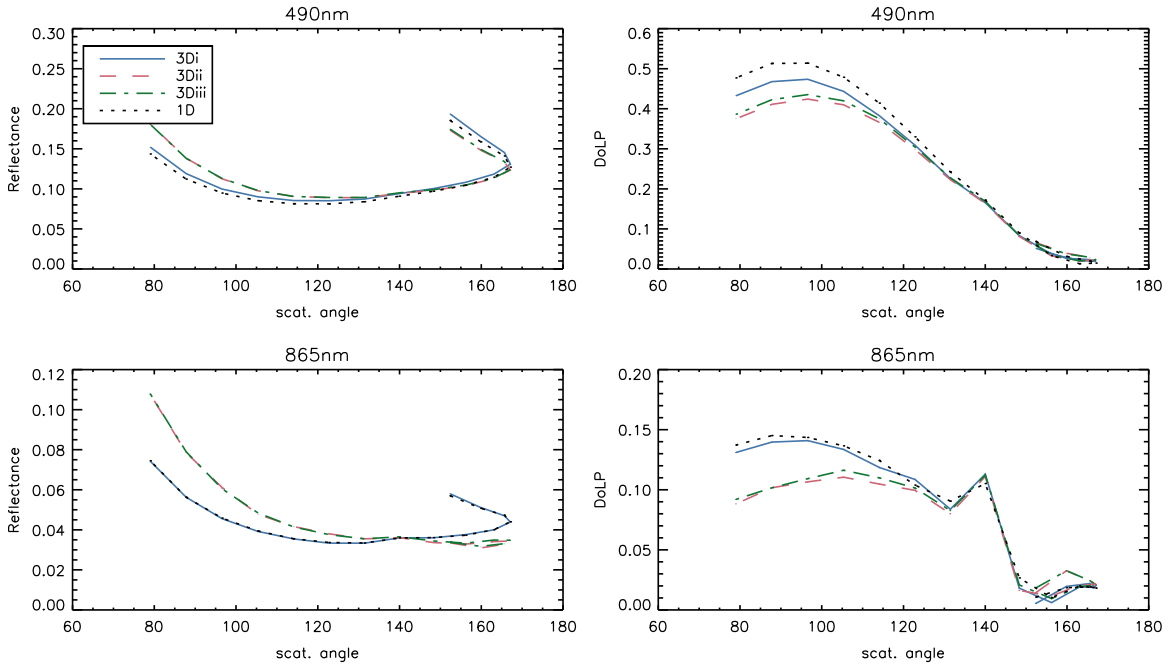

Fig. 8. Comparison of 3D 'edge' models at three different viewing geometries (see Table 2) and their 1D counterpart. This scene, of MR PARASOL ground pixel size, has 10% cloud cover between 1.5 and 1.6 km with a COT of $\tau_{550\,\mathrm{nm}}^{\mathrm{cloud}} = 10.0$.

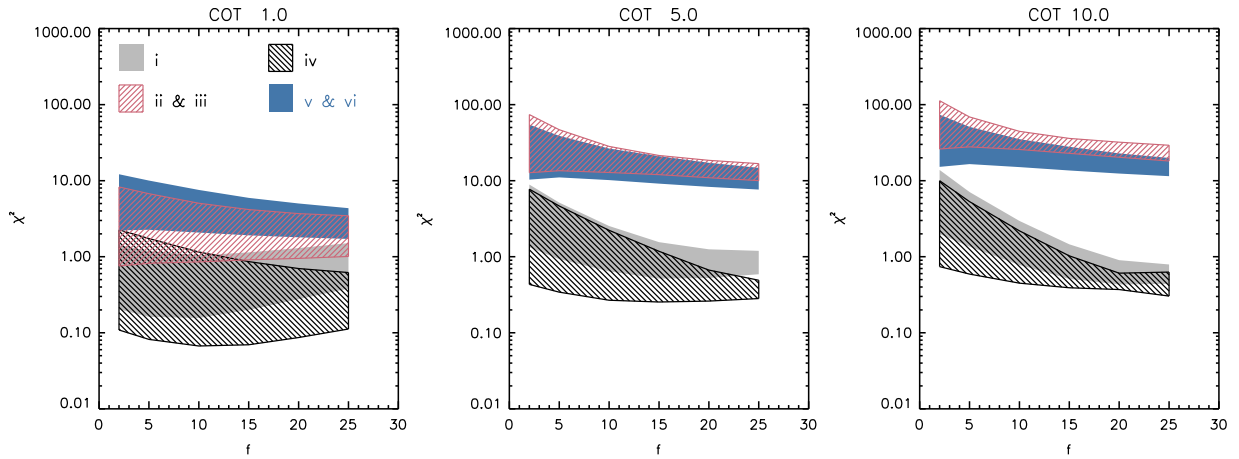

Fig. 9. Quantifies the 3D effects in terms of χ^2 for the edge cloud models (with a vertical cloud profile between 1.5 and 1.6 km) as a function of cloud fraction. The vertical range in each polygon is due to the different aerosol loads of the models and (if applicable) the different solar azimuth angles.

The viewing geometries (*ii*, *iii*, *v* and *vi*) cause large differences between the synthetic measurements of the 1D and 3D models, even at low cloud fractions. This is clear from the in general one order of magnitude larger χ^2 difference with the 1D models in Fig. 9 for these geometries. These differences become larger for increasing COT. In these geometries the SZA is more important (geometries *ii* and *iii* versus geometries *v* and *vi*) than whether or not the side of the cloud is illuminated (geometries *ii* and *v* versus *iii* and *vi*). The net 3D effect, for all geometries, only marginally increases, or even decreases with increasing cloud fraction.

For the FR pixels there are larger differences between the 3D and 1D models. This can be explained by the fact that the volume of air that is near the cloud is relatively larger. Furthermore, the shadow fraction is relatively larger (in scenes with geometries are *i* and *iv*) and there is a relatively larger fraction of cloud where darkening of the cloud edge is important. The forward model error is roughly twice as large in the FR measurements compared to the MR measurements.

4.2. 3D effects on retrieved aerosol properties

4.2.1. Broken cloud fields

Retrievals are performed for all the FR scenes with clouds with horizontal dimensions of 100×100 m, as discussed in Section 3.1. These scenes vary in aerosol type

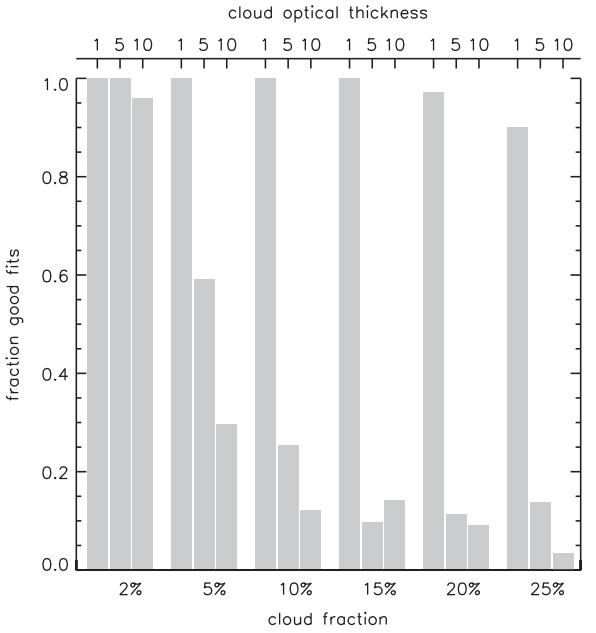

Fig. 10. Histogram of the fraction of retrievals of the broken cloud field scenes that meet the $\chi^2 \leq 2.0$ criterion. The histogram is divided by cloud fraction and COT.

and load, COT, vertical cloud profile, solar zenith and azimuth angle, viewing geometry and cloud fraction. Since the retrieval algorithm employs a 1D forward model with IPA, it is expected that the algorithm will adjust the 1D IPA cloud parameters and aerosol parameters to compensate for 3D effects.

Fig. 10 shows the fraction of retrievals that converge successfully ($\chi^2 < 2.0$), for different values of COT and cloud fraction. For the lowest COT, it is in most cases possible to obtain a good fit with the 1D forward model used in the retrieval, even for a cloud fraction of 25%. At COTs of $\tau^{\text{cloud}}_{550\text{ nm}} \geq 5.0$ the fraction of good fits decreases with increasing cloud fraction, because of increasing importance of 3D effects.

Fig. 11 compares the retrieved aerosol parameters for successfully converged retrievals to the true parameters used to create the synthetic 3D measurement. This is done via box-and-whisker diagrams which indicate the minimum, 1st quartile, the median, the 3rd quartile and the maximum of all retrieved values for every true value. Overall the retrieved AOT is close to the truth, with a very narrow distribution. The scatter in retrieved SSA is larger, but the 1st to 3rd quartile is still close to the truth. However, there are a number of significant outliers to higher values and an overall bias to lower values when the SSA is low. Similarly, for the m_r of both the fine and the coarse mode, the comparison is good in general but there are a number of outliers to high and low values.

In Table 3 the bias and standard deviation for the difference between retrieved and true parameters are separately shown per cloud fraction and optical thickness for the successfully converged retrievals. There is a bias towards underestimated AOT that increases with increasing cloud fraction and COT. In Fig. 11 these cases represent the outliers. For the SSA there is a bias towards overestimation in the models with $\tau^{\text{cloud}}_{550\text{ nm}} \geq 5.0$ and $f \geq 0.15$. The standard deviation of the retrieved real part of the complex refractive index of both the fine and the coarse mode becomes larger than 0.02 in scenes with $\tau^{\text{cloud}}_{550\text{ nm}} \geq 5.0$ and $f \geq 0.15$.

Mishchenko et al. [37] formulated the following accuracy requirements on aerosol properties for climate research in the context of the Aerosol Polarimetry Sensor (APS): 0.02 or 7% for the AOT for over ocean scenes, 0.03 on the SSA, 0.02 on the m_r and 0.1 μm on r_{eff} for each mode. When we consider these requirements, we conclude from Table 3 that if $\tau^{\text{cloud}}_{550\text{ nm}} = 1$, a 1D forward model with the IPA can be used to retrieve aerosol properties with sufficient accuracy, even for cloud fractions up to 25%, for a broken cloud field with randomly distributed clouds. For optically thicker clouds 3D effects become, as expected, more important. For $\tau^{\text{cloud}}_{550\text{ nm}} \geq 5$, 3D effects can only be ignored for small cloud fractions (10% or less).

The retrieval results presented in this study are obtained under the assumption of perfect a priori knowledge of the cloud droplet size. While this is useful for studying the influence of 3D effects, it may not be realistic in actual observations of partially clouded scenes. Therefore, the retrievals have also been performed for several incorrect effective radii for the cloud droplets ($r^{\text{cloud}}_{\text{eff}}$). When instead of the true droplet size ($r^{\text{cloud}}_{\text{eff}} = 12.0$ μm) an incorrect $r^{\text{cloud}}_{\text{eff}} = 9.0$ μm is assumed, the fractions of good fits found for all COT and $f \leq 10\%$ remain equal. At low COT and $f > 10\%$ the fraction of good fits is decreased by 0.1 at $f = 15\%$ and by 0.2 at $f = 25\%$. At $\tau^{\text{cloud}}_{550\text{ nm}} \geq 5.0$ and $f > 10\%$ the fractions of good fits are already low (see Fig. 10) and they decrease by ~ 0.01. The retrieved optical and microphysical parameters at $\tau^{\text{cloud}}_{550\text{ nm}} = 1$ and at $\tau^{\text{cloud}}_{550\text{ nm}} \geq 5.0$ with $f \leq 5\%$ are still in agreement with the accuracy requirements. When the retrievals are performed with a particularly poor a priori assumption of $r^{\text{cloud}}_{\text{eff}} = 6.0$ μm, the fractions of good fits decrease by 0.1 at $\tau^{\text{cloud}}_{550\text{ nm}} = 1.0$ and $f = 5\%$ and by 0.6 at $\tau^{\text{cloud}}_{550\text{ nm}} = 1$ and $f = 25\%$. Even here, the AOT, SSA and r_{eff} of both modes are still in agreement within the accuracy requirements at $\tau^{\text{cloud}}_{550\text{ nm}} = 1$ and at $\tau^{\text{cloud}}_{550\text{ nm}} \geq 5.0$ with $f \leq 5\%$. The retrieved m_r of both modes, however, show more scatter and a bias that is larger than the accuracy requirements.

4.2.2. Cloud edge cases

Retrievals are performed for all the MR scenes described in Section 3.2. These scenes vary in aerosol type and load, COT, vertical cloud profile, solar zenith and azimuth angle, viewing geometry and cloud fraction. Fig. 12 shows the fraction of retrievals that converge successfully ($\chi^2 < 2.0$), for different values of COT and cloud fraction, separated by geometry. For low COT ($\tau^{\text{cloud}}_{550\text{ nm}} = 1.0$) the 1D algorithm has no difficulty in obtaining a fit since the 3D effects are small (see Fig. 9). At $\tau^{\text{cloud}}_{550\text{ nm}} \geq = 5.0$, the viewing geometry is of particular importance. For geometries *ii*, *iii*, *v* and *vi* the cloud fraction varies between the viewing angles and the algorithm is not able to reproduce radiances of these measurements. Remarkably, the fraction of good fits remains constant with increasing cloud fractions for synthetic measurements with viewing geometries *i*

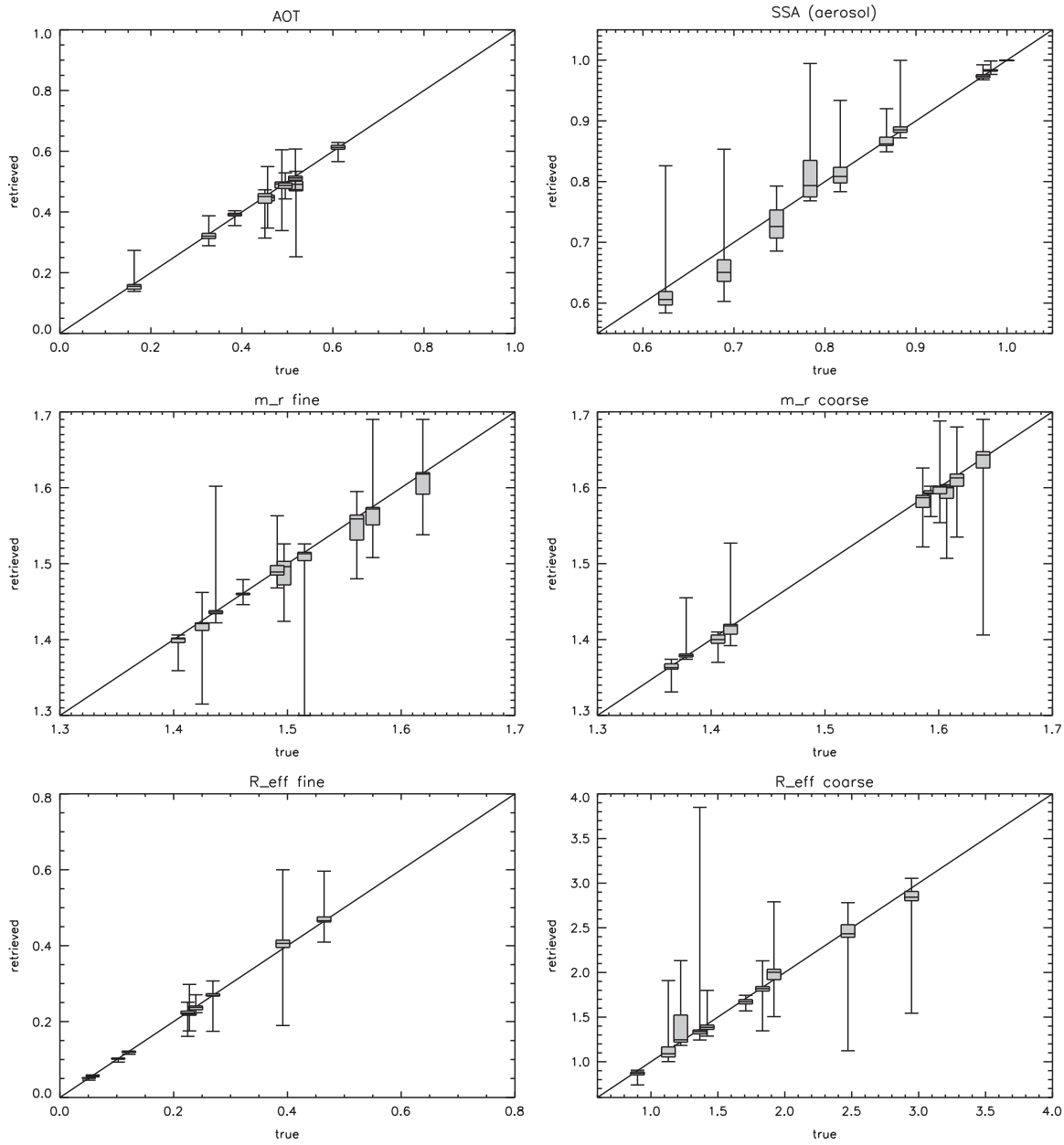

Fig. 11. Box-and-whisker diagrams for the true versus retrieved values in the broken cloud field scenes. The whiskers indicate the minimum and maximum ranges of the retrieved parameter. The boxes indicate the 1st, 2nd and 3rd quartile of the retrieved parameter. Only retrievals with $\chi^2 \leq 2.0$ are included.

and *iv*. This can be explained as the 3D effects at these geometries (shadow, cloud induced enhancements of the cloud free column and cloud edge darkening) have opposite effects and cause systematic, but modest differences with the 1D models (see Fig. 9).

A comparison of the true and retrieved parameters, for all edge cloud retrievals that successfully converged ($\chi^2 \leq 2.0$), is given in Fig. 13. Like for the broken cloud field retrievals of Fig. 11, the scatter is shown via box-and-whisker diagrams. In general, the error on the aerosol parameters caused by 3D effects is significantly larger than for scenes with broken, randomly distributed clouds (see Fig. 11). For some cases the AOT tends to be underestimated, the SSA overestimated, the m_r of the coarse mode underestimated and the effective radius of the coarse mode underestimated.

In Tables 4 and 5 the bias and standard deviations of the difference between retrieved and true parameters are separately shown per COT, cloud fraction and solar zenith angle. From Tables 4 and 5 it follows that for SZA=40°, 3D effects do not significantly hamper aerosol retrievals for partly cloudy scenes with $\tau^{\text{cloud}}_{550\text{ nm}} = 1$, while for SZA=60° only the AOT can be retrieved with sufficient accuracy when the $\tau^{\text{cloud}}_{550\text{ nm}} \leq 5$ and $f \leq 10\%$. For larger COT the errors caused by 3D effects are too large compared to the

Table 3
Statistics from the broken cloud field retrievals, for a selection of retrieved optical and micro-physical parameters, separated by cloud fraction and COT. Column 2 lists the number of good fits. Columns 3-6 list the mean and, between parenthesis, the standard deviation of the difference in the true and retrieved AOT, SSA and real refractive indices of both modes.

	n	ΔAOT	ΔSSA	Δm_r^f	Δm_r^c
$\tau_{550\,nm}^{cloud}=1.0$, $f=2\%$	240	−0.002 (0.010)	−0.006 (0.007)	−0.001 (0.006)	0.000 (0.004)
$\tau_{550\,nm}^{cloud}=1.0$, $f=5\%$	240	−0.002 (0.008)	−0.009 (0.009)	−0.001 (0.005)	0.001 (0.004)
$\tau_{550\,nm}^{cloud}=1.0$, $f=10\%$	240	−0.005 (0.012)	−0.013 (0.015)	−0.001 (0.005)	0.002 (0.005)
$\tau_{550\,nm}^{cloud}=1.0$, $f=15\%$	240	−0.007 (0.014)	−0.016 (0.018)	−0.002 (0.005)	0.002 (0.006)
$\tau_{550\,nm}^{cloud}=1.0$, $f=20\%$	233	−0.010 (0.016)	−0.018 (0.021)	−0.001 (0.003)	0.002 (0.006)
$\tau_{550\,nm}^{cloud}=1.0$, $f=25\%$	216	−0.012 (0.017)	−0.020 (0.024)	−0.001 (0.004)	0.002 (0.006)
$\tau_{550\,nm}^{cloud}=5.0$, $f=2\%$	240	−0.004 (0.012)	0.003 (0.011)	−0.016 (0.016)	−0.016 (0.013)
$\tau_{550\,nm}^{cloud}=5.0$, $f=5\%$	142	−0.005 (0.015)	0.002 (0.013)	−0.019 (0.017)	−0.015 (0.011)
$\tau_{550\,nm}^{cloud}=5.0$, $f=10\%$	61	−0.020 (0.018)	0.001 (0.009)	−0.014 (0.015)	−0.015 (0.010)
$\tau_{550\,nm}^{cloud}=5.0$, $f=15\%$	23	−0.071 (0.076)	0.042 (0.057)	−0.015 (0.015)	−0.004 (0.023)
$\tau_{550\,nm}^{cloud}=5.0$, $f=20\%$	27	−0.074 (0.092)	0.082 (0.081)	−0.004 (0.027)	0.007 (0.063)
$\tau_{550\,nm}^{cloud}=5.0$, $f=25\%$	33	−0.049 (0.088)	0.054 (0.064)	0.019 (0.052)	0.030 (0.041)
$\tau_{550\,nm}^{cloud}=10.0$, $f=2\%$	230	−0.000 (0.024)	0.024 (0.024)	−0.020 (0.034)	−0.012 (0.019)
$\tau_{550\,nm}^{cloud}=10.0$, $f=5\%$	71	−0.009 (0.051)	0.022 (0.037)	−0.019 (0.030)	−0.010 (0.023)
$\tau_{550\,nm}^{cloud}=10.0$, $f=10\%$	29	−0.059 (0.108)	0.063 (0.068)	−0.034 (0.075)	−0.031 (0.048)
$\tau_{550\,nm}^{cloud}=10.0$, $f=15\%$	34	−0.105 (0.091)	0.072 (0.080)	−0.005 (0.053)	−0.018 (0.059)
$\tau_{550\,nm}^{cloud}=10.0$, $f=20\%$	22	−0.111 (0.116)	0.095 (0.082)	−0.022 (0.040)	−0.033 (0.056)
$\tau_{550\,nm}^{cloud}=10.0$, $f=25\%$	8	−0.119 (0.051)	0.090 (0.010)	−0.037 (0.072)	−0.032 (0.007)

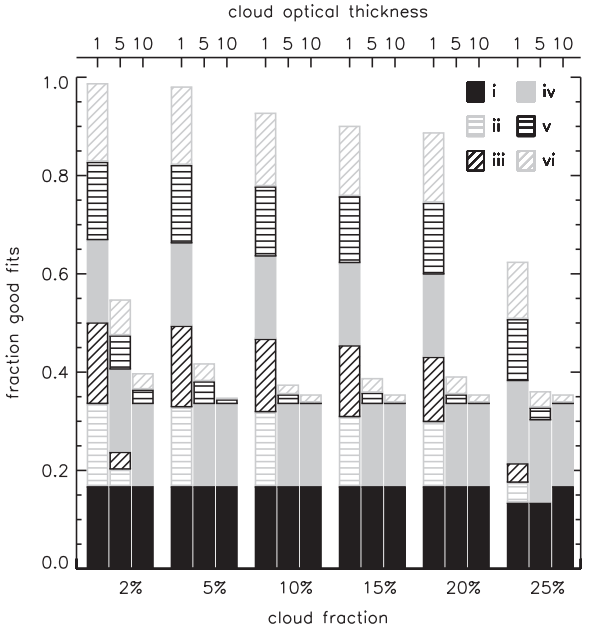

Fig. 12. The histogram shows, for each cloud fraction and COT, in what fraction of the MR 'edge' cases a fit with $\chi^2 \leq 2.0$ is obtained. The fractions have been further divided by geometry (see Table 2) by use of hatching and colors.

requirements. For SZA=40° and $\tau_{550\,nm}^{cloud} \geq 5$, only the m_r of the coarse mode can be retrieved with sufficient accuracy.

Considering that the forward model error due to neglecting 3D effects is roughly twice as large in the FR compared to the MR 'edge' cases (as described in Section 4.1.2) and that in the MR 'edge' cases the retrieved aerosol properties only meet the accuracy requirements for $\tau_{550\,nm}^{cloud}=1$ and SZA=40°, larger errors and biases in the retrieved aerosol properties are expected at this higher resolution. Therefore we refrain from performing and the analyzing the retrievals on the FR 'edge' cases.

5. Conclusions and discussion

We investigated the importance of 3D radiative transfer effects on simultaneous aerosol and cloud retrievals in scenes with partial, liquid water cloud cover. Hereto, we created synthetic, multi-wavelength, multi-angular, photo-polarimetric measurements with the 3D radiative transfer model MYSTIC and performed retrievals using a 1D radiative transfer model based on the independent pixel approximation.

In the random cloud distributions the synthetic measurements show systematic differences with the 1D forward model due to 3D effects even for small cloud fractions. The 3D effects mostly affect the intensity which can easily range up to 20% for a scene with COT of $\tau_{550\,nm}^{cloud}=5.0$ and $f=5\%$. At higher COT and higher cloud fraction these differences become larger.

In the 'edge' cases, the differences in synthetic measurements of 1D and 3D scenes are dominated by the viewing geometry. In worst case, the differences in intensity can range up to 25% for scenes with a small cloud fraction and low optical thickness ($f=2\%$ and $\tau_{550\,nm}^{cloud}=1.0$). For fortunate viewing geometries these differences in intensity are generally of the order of a few percent, ranging up to 10%. For these 'edge' cases, the influence of the 3D effects does not strongly depend on cloud fraction.

In the broken cloud fields, the retrieval algorithm is able to obtain a fit for scenes with clouds of low COT at all

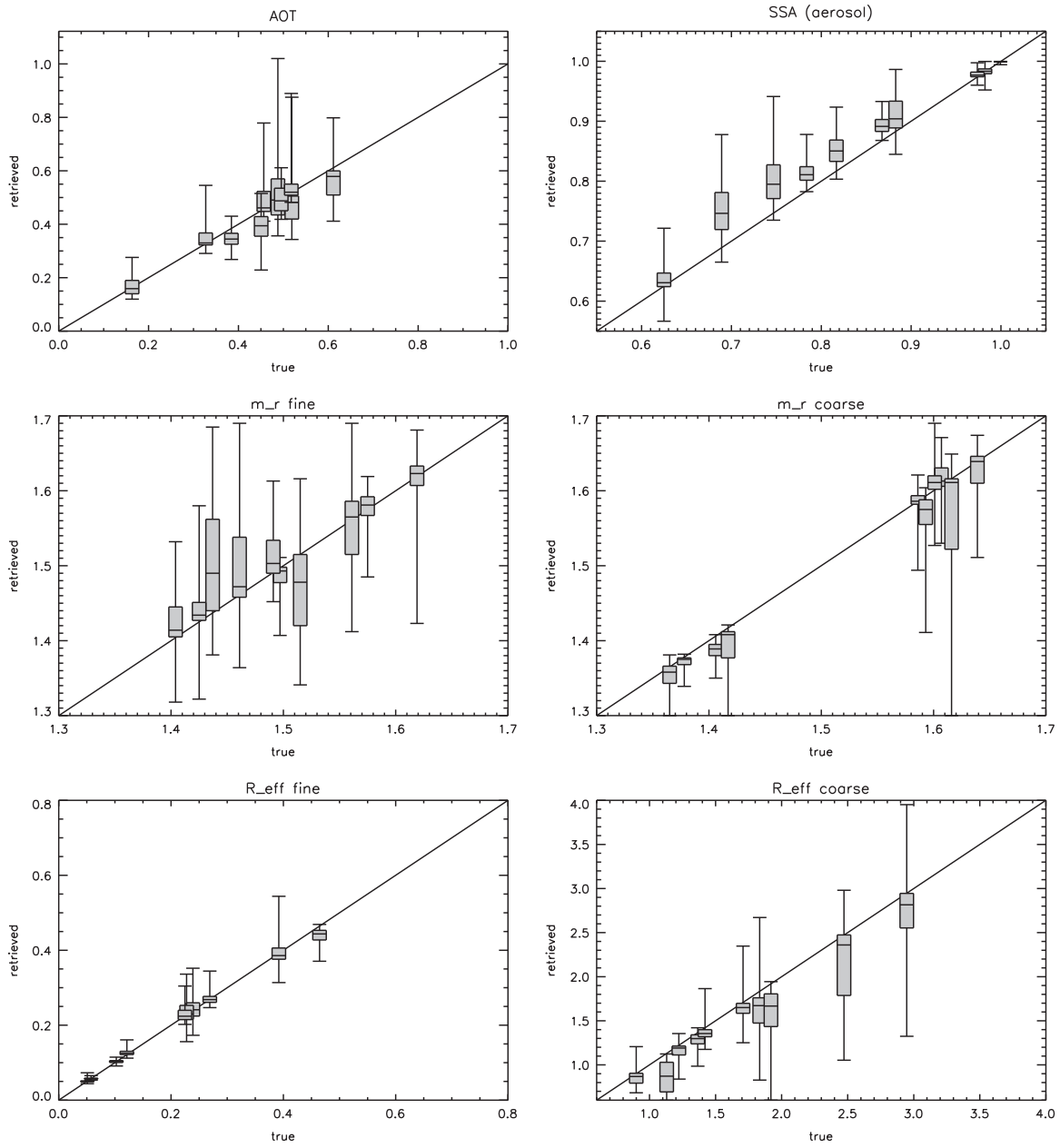

Fig. 13. Box-and-whisker diagrams for the true versus retrieved values in the edge cloud field scenes. The whiskers indicate the minimum and maximum ranges of the retrieved parameter. The boxes indicate the 1st, 2nd and 3rd quartile of the retrieved parameter. Only retrievals with $\chi^2 \leq 2.0$ are included.

cloud fractions and for scenes with $\tau^{\text{cloud}}_{550\text{ nm}} \geq 5.0$ at low cloud fraction. At low COT this fit is obtained by adjusting the 1D IPA cloud parameters, without significantly altering the aerosol parameters. This indicates that the 3D effects are not misinterpreted as aerosol signal and thus that 1D RT is sufficient for retrieving the aerosol optical and microphysical properties in the vicinity of random, liquid water cloud distributions of low optical thickness. At $\tau^{\text{cloud}}_{550\text{ nm}} \geq 5.0$ the aerosol parameters are somewhat adjusted to account for the 3D influence in the synthetic measurements. At low cloud fractions ($f \leq 5\%$) the retrievals still meet the accuracy requirements on the AOT, the SSA and the m_r of each mode. The retrieved optical and microphysical aerosol parameters for scenes with a random cloud distribution, $\tau^{\text{cloud}}_{550\text{ nm}} \geq 5.0$ combined with a cloud fraction larger than 5% do not meet the required accuracies.

In observations of scenes with non-random cloud distributions, such as the 'edge' cases, the algorithm is able to obtain a fit when the viewing geometry is optimal (i.e. when cloud fraction is constant at all viewing angles) or when the COT is low ($\tau^{\text{cloud}}_{550\text{ nm}} = 1.0$). Although the retrieved aerosol properties in the 'edge' cases with $\tau^{\text{cloud}}_{550\text{ nm}} = 1.0$ and $f \leq 20\%$ do not meet the accuracy

Table 4
Statistics from the edge cloud model retrievals with $\theta_{sun} = 40.0^{\circ}$, for a selection of retrieved optical and micro-physical parameters, separated by cloud fraction and COT. Column 2 lists the number retrievals that pass the χ^2−filter. Columns 3-6 list the mean and, between parenthesis, the standard deviation of the difference in the true and retrieved AOT, SSA and real refractive indices of both modes.

	n	ΔAOT	ΔSSA	Δm_r^f	Δm_r^c
$\tau_{550\ nm}^{cloud} = 1.0, f = 2\%$	150	−0.003 (0.030)	0.025 (0.026)	−0.003 (0.034)	−0.010 (0.019)
$\tau_{550\ nm}^{cloud} = 1.0, f = 5\%$	148	0.001 (0.029)	0.019 (0.027)	0.001 (0.025)	−0.011 (0.022)
$\tau_{550\ nm}^{cloud} = 1.0, f = 10\%$	140	0.004 (0.029)	0.013 (0.022)	0.002 (0.019)	−0.011 (0.020)
$\tau_{550\ nm}^{cloud} = 1.0, f = 15\%$	136	−0.002 (0.024)	0.012 (0.019)	0.002 (0.008)	−0.009 (0.015)
$\tau_{550\ nm}^{cloud} = 1.0, f = 20\%$	129	−0.002 (0.020)	0.008 (0.013)	0.002 (0.006)	−0.007 (0.012)
$\tau_{550\ nm}^{cloud} = 1.0, f = 25\%$	64	−0.011 (0.016)	−0.003 (0.005)	0.003 (0.005)	−0.005 (0.004)
$\tau_{550\ nm}^{cloud} = 5.0, f = 2\%$	71	0.000 (0.118)	0.047 (0.042)	0.038 (0.062)	−0.013 (0.041)
$\tau_{550\ nm}^{cloud} = 5.0, f = 5\%$	50	−0.062 (0.047)	0.041 (0.030)	0.044 (0.034)	0.002 (0.015)
$\tau_{550\ nm}^{cloud} = 5.0, f = 10\%$	50	−0.054 (0.041)	0.031 (0.023)	0.030 (0.029)	−0.001 (0.009)
$\tau_{550\ nm}^{cloud} = 5.0, f = 15\%$	50	−0.046 (0.035)	0.022 (0.018)	0.023 (0.022)	−0.002 (0.010)
$\tau_{550\ nm}^{cloud} = 5.0, f = 20\%$	50	−0.041 (0.032)	0.013 (0.013)	0.018 (0.020)	−0.000 (0.011)
$\tau_{550\ nm}^{cloud} = 5.0, f = 25\%$	40	−0.028 (0.019)	−0.002 (0.010)	0.004 (0.009)	−0.008 (0.016)
$\tau_{550\ nm}^{cloud} = 10.0, f = 2\%$	50	−0.089 (0.071)	0.067 (0.046)	0.078 (0.055)	0.002 (0.018)
$\tau_{550\ nm}^{cloud} = 10.0, f = 5\%$	50	−0.080 (0.065)	0.056 (0.040)	0.059 (0.047)	0.000 (0.017)
$\tau_{550\ nm}^{cloud} = 10.0, f = 10\%$	50	−0.070 (0.057)	0.042 (0.032)	0.039 (0.038)	−0.001 (0.011)
$\tau_{550\ nm}^{cloud} = 10.0, f = 15\%$	50	−0.051 (0.044)	0.026 (0.022)	0.023 (0.030)	−0.001 (0.010)
$\tau_{550\ nm}^{cloud} = 10.0, f = 20\%$	50	−0.034 (0.033)	0.011 (0.011)	0.014 (0.026)	−0.001 (0.013)
$\tau_{550\ nm}^{cloud} = 10.0, f = 25\%$	50	−0.005 (0.013)	0.002 (0.004)	0.001 (0.002)	−0.000 (0.001)

Table 5
The same as Table 4 but for $\theta_{sun} = 60.0^{\circ}$.

	n	ΔAOT	ΔSSA	Δm_r^f	Δm_r^c
$\tau_{550\ nm}^{cloud} = 1.0, f = 2\%$	146	0.005 (0.039)	0.034 (0.037)	−0.021 (0.058)	−0.024 (0.044)
$\tau_{550\ nm}^{cloud} = 1.0, f = 5\%$	146	0.009 (0.045)	0.032 (0.038)	−0.022 (0.051)	−0.027 (0.045)
$\tau_{550\ nm}^{cloud} = 1.0, f = 10\%$	138	0.017 (0.044)	0.026 (0.037)	−0.017 (0.041)	−0.031 (0.044)
$\tau_{550\ nm}^{cloud} = 1.0, f = 15\%$	134	0.022 (0.045)	0.020 (0.031)	−0.022 (0.040)	−0.025 (0.038)
$\tau_{550\ nm}^{cloud} = 1.0, f = 20\%$	137	0.024 (0.046)	0.021 (0.037)	−0.020 (0.039)	−0.028 (0.047)
$\tau_{550\ nm}^{cloud} = 1.0, f = 25\%$	123	0.047 (0.046)	0.022 (0.031)	−0.046 (0.048)	−0.037 (0.046)
$\tau_{550\ nm}^{cloud} = 5.0, f = 2\%$	93	0.006 (0.094)	0.044 (0.042)	0.014 (0.083)	−0.029 (0.061)
$\tau_{550\ nm}^{cloud} = 5.0, f = 5\%$	75	0.003 (0.106)	0.036 (0.038)	0.022 (0.075)	−0.019 (0.051)
$\tau_{550\ nm}^{cloud} = 5.0, f = 10\%$	62	−0.014 (0.109)	0.028 (0.024)	0.033 (0.073)	−0.002 (0.024)
$\tau_{550\ nm}^{cloud} = 5.0, f = 15\%$	66	0.010 (0.141)	0.024 (0.029)	0.026 (0.070)	−0.008 (0.040)
$\tau_{550\ nm}^{cloud} = 5.0, f = 20\%$	67	0.020 (0.131)	0.021 (0.033)	0.023 (0.071)	−0.011 (0.039)
$\tau_{550\ nm}^{cloud} = 5.0, f = 25\%$	68	0.062 (0.153)	0.023 (0.029)	−0.003 (0.094)	−0.015 (0.040)
$\tau_{550\ nm}^{cloud} = 10.0, f = 2\%$	69	−0.025 (0.102)	0.047 (0.036)	0.041 (0.095)	−0.015 (0.049)
$\tau_{550\ nm}^{cloud} = 10.0, f = 5\%$	54	−0.056 (0.086)	0.038 (0.028)	0.049 (0.087)	−0.003 (0.030)
$\tau_{550\ nm}^{cloud} = 10.0, f = 10\%$	56	−0.040 (0.106)	0.032 (0.027)	0.050 (0.082)	−0.007 (0.037)
$\tau_{550\ nm}^{cloud} = 10.0, f = 15\%$	56	−0.025 (0.129)	0.026 (0.025)	0.042 (0.075)	−0.001 (0.024)
$\tau_{550\ nm}^{cloud} = 10.0, f = 20\%$	56	−0.019 (0.128)	0.019 (0.023)	0.040 (0.077)	−0.001 (0.026)
$\tau_{550\ nm}^{cloud} = 10.0, f = 25\%$	56	0.007 (0.122)	0.018 (0.026)	0.023 (0.060)	−0.016 (0.060)

requirements they are still reasonable. At higher COT a bias is introduced in the retrieved AOT, SSA, m_r and r_{eff} of the coarse mode. This indicates that for $\tau_{550\ nm}^{cloud} > 1$, 1D RT is not sufficient for retrieving aerosol properties in scenes with liquid water clouds concentrated at the edge of a ground pixel.

The simulated clouds used in this study are simple cuboids and homogeneous slabs that, contrary to realistic clouds, have smooth surfaces and micro-physical properties that remain constant throughout the cloud. This simplification of the clouds allows us to create a large data set that enables us to systematically investigate the influences of shadows, illumination of the cloud free column and illumination of the sides of the clouds for different viewing geometries, cloud distributions, cloud fractions, cloud heights and geometrical thicknesses.

If one wants to retrieve aerosol properties in scenes with $\tau_{550\ nm}^{cloud} \geq 5.0$ and $f \geq 5\%$ or scenes with clouds concentrated at the edge of the ground pixel, steps should be taken to expand the forward models to at least account for 3D effects as proposed by [38].

References

[1] Intergovernmental panel on climate change. Fifth assessment report: climate change 2013. The Physical Science Basis; 2014.

[2] Mishchenko MI, Travis LD. Satellite retrieval of aerosol properties over the ocean using polarization as well as intensity of reflected sunlight. J Geophys Res-Atmos 1997;102:16989. http://dx.doi.org/10.1029/96JD02425.

[3] Hasekamp OP, Landgraf J. Retrieval of aerosol properties over land surfaces: capabilities of multiple-viewing-angle intensity and polarization measurements. Appl Opt 2007;46:3332–44. http://dx.doi.org/10.1364/AO.46.003332.

[4] Kokhanovsky AA, Deuzé JL, Diner DJ, Dubovik O, Ducos F, Emde C, et al. The inter-comparison of major satellite aerosol retrieval algorithms using simulated intensity and polarization characteristics of reflected light. Atmos Meas Tech 2010;3:909–32.

[5] Knobelspiesse K, Cairns B, Mishchenko M, Chowdhary J, Tsigaridis K, van Diedenhoven B, et al. Analysis of fine-mode aerosol retrieval capabilities by different passive remote sensing instrument designs. Opt Express 2012;20:21457. http://dx.doi.org/10.1364/OE.20.021457.

[6] Ottaviani M, Knobelspiesse K, Cairns B, Mishchenko M. Information content of aerosol retrievals in the sunglint region. Geophys Res Lett 2013;40:631–4. http://dx.doi.org/10.1002/grl.50148.

[7] Chowdhary J, Cairns B, Mishchenko MI, Hobbs PV, Cota GF, Redemann J, et al. Retrieval of aerosol scattering and absorption properties from photopolarimetric observations over the ocean during the CLAMS experiment. J Atmos Sci 2005;62:1093–117. http://dx.doi.org/10.1175/JAS3389.1.

[8] Waquet F, Cairns B, Knobelspiesse K, Chowdhary J, Travis LD, Schmid B, et al. Polarimetric remote sensing of aerosols over land. J Geophys Res-Atmos 2009;114:1206. http://dx.doi.org/10.1029/2008JD010619.

[9] Wu L, Hasekamp O, van Diedenhoven B, Cairns B. Aerosol retrieval from multiangle, multispectral photopolarimetric measurements: importance of spectral range and angular resolution. Atmos Meas Tech 2015;8:2625–38. http://dx.doi.org/10.5194/amt-8-2625-2015.

[10] Dubovik O, Herman M, Holdak A, Lapyonok T, Tanré D, Deuzé JL, et al. Statistically optimized inversion algorithm for enhanced retrieval of aerosol properties from spectral multi-angle polarimetric satellite observations. Atmos Meas Tech 2011;4:975–1018. http://dx.doi.org/10.5194/amt-4-975-2011.

[11] Hasekamp OP, Litvinov P, Butz A. Aerosol properties over the ocean from PARASOL multiangle photopolarimetric measurements. J Geophys Res-Atmos 2011;116:14204. http://dx.doi.org/10.1029/2010JD015469.

[12] Waquet F, Cornet C, Deuzé J-L, Dubovik O, Ducos F, Goloub P, et al. Retrieval of aerosol microphysical and optical properties above liquid clouds from POLDER/PARASOL polarization measurements. Atmos Meas Tech 2013;6:991–1016. http://dx.doi.org/10.5194/amt-6-991-2013.

[13] Koren I, Remer LA, Kaufman YJ, Rudich Y, Martins JV. On the twilight zone between clouds and aerosols. Geophys Res Lett 2007;34:8805. http://dx.doi.org/10.1029/2007GL029253.

[14] Charlson RJ, Ackerman AS, Bender FA-M, Anderson TL, Liu Z. On the climate forcing consequences of the albedo continuum between cloudy and clear air. Tellus Ser B Chem Phys Meteorol B 2007;59:715–27. http://dx.doi.org/10.1111/j.1600-0889.2007.00297.x.

[15] Redemann J, Zhang Q, Russell PB, Livingston JM, Remer LA. Case studies of aerosol remote sensing in the vicinity of clouds. J Geophys Res-Atmos 114 (D6), 2009.

[16] Wen G, Marshak A, Cahalan RF, Remer LA, Kleidman RG. 3-d aerosol-cloud radiative interaction observed in collocated modis and aster images of cumulus cloud fields. J Geophys Res-Atmos 2007;112(D13):d13204. http://dx.doi.org/10.1029/2006JD008267.

[17] Várnai T, Marshak A. Modis observations of enhanced clear sky reflectance near clouds. Geophys Res Lett 2009;36(6):l06807. http://dx.doi.org/10.1029/2008GL037089.

[18] Stap FA, Hasekamp OP, Röckmann T. Sensitivity of PARASOL multi-angle photopolarimetric aerosol retrievals to cloud contamination. Atmos Meas Tech 2015;8:1287–301. http://dx.doi.org/10.5194/amt-8-1287-2015.

[19] Hasekamp OP. Capability of multi-viewing-angle photo-polarimetric measurements for the simultaneous retrieval of aerosol and cloud properties. Atmos Meas Tech 2010;3:839–51.

[20] Waquet F, Riedi J, Labonnote LC, Goloub P, Cairns B, Deuzé J-L, et al. Aerosol remote sensing over clouds using a-train observations. J Atmos Sci 2009;66:2468. http://dx.doi.org/10.1175/2009JAS3026.1.

[21] Marshak A, Wen G, Coakley JA, Remer LA, Loeb NG, Cahalan RF. A simple model for the cloud adjacency effect and the apparent bluing of aerosols near clouds. J Geophys Res-Atmos 2008;113:14. http://dx.doi.org/10.1029/2007JD009196.

[22] Davis AB, Garay MJ, Xu F, Qu Z, Emde C. 3D radiative transfer effects in multi-angle/multispectral radio-polarimetric signals from a mixture of clouds and aerosols viewed by a non-imaging sensor. In: Society of photo-optical instrumentation engineers (SPIE) conference series, vol. 8873, 2013. p. 9, http://dx.doi.org/10.1117/12.2023733.

[23] Hansen JE, Travis LD. Light scattering in planetary atmospheres. Space Sci Rev 1974;16:527–610. http://dx.doi.org/10.1007/BF00168069.

[24] Di Noia A, Hasekamp OP, van Harten G, Rietjens JHH, Smit JM, Snik F, et al. Use of neural networks in ground-based aerosol retrievals from multi-angle spectropolarimetric observations. Atmos Meas Tech 2015;8:281–99. http://dx.doi.org/10.5194/amt-8-281-2015.

[25] Dubovik O, Sinyuk A, Lapyonok T, Holben BN, Mishchenko M, Yang P, et al. Application of spheroid models to account for aerosol particle nonsphericity in remote sensing of desert dust. J Geophys Res Atmos 2006;111:11208. http://dx.doi.org/10.1029/2005JD006619.

[26] Segelstein D. The complex refractive index of water. Kansas City: Department of Physics, University of Missouri-Kansas City; 1981.

[27] Landgraf J, Hasekamp OP, Box MA, Trautmann T. A linearized radiative transfer model for ozone profile retrieval using the analytical forward-adjoint perturbation theory approach. J Geophys Res-Atmos 2001;106:27291. http://dx.doi.org/10.1029/2001JD000636.

[28] Hasekamp OP, Landgraf J. A linearized vector radiative transfer model for atmospheric trace gas retrieval. J Quant Spectrosc Radiat 2002;75:
221–38. http://dx.doi.org/10.1016/S0022-4073(01)00247-3.

[29] Hasekamp OP, Landgraf J. Linearization of vector radiative transfer with respect to aerosol properties and its use in satellite remote sensing. J Geophys Res-Atmos 2005;110:4203. http://dx.doi.org/10.1029/2004JD005260.

[30] Nakajima T, Tanaka M. Algorithms for radiative intensity calculations in moderately thick atmospheres using a truncation approximation. J Quant Spectrosc Radiat 1988;40:51–69. http://dx.doi.org/10.1016/0022-4073(88)90031-3.

[31] Mayer B. Radiative transfer in the cloudy atmosphere. In: European physical journal web of conferences. vol. 1, 2009. p. 75, http://dx.doi.org/10.1140/epjconf/e2009-00912-1.

[32] Emde C, Mayer B. Simulation of solar radiation during a total eclipse: a challenge for radiative transfer. Atmos Chem Phys 2007;7:2259–70.

[33] Emde C, Buras R, Mayer B, Blumthaler M. The impact of aerosols on polarized sky radiance: model development, validation, and applications. Atmos Chem Phys 2010;10:383–96.

[34] Mayer B, Kylling A. Technical note: the libradtran software package for radiative transfer calculations – description and examples of use. Atmos Chem Phys 2005;5(7):1855–77.

[35] Marshak A, Davis A. 3D radiative transfer in cloudy atmospheres. Physics of earth and space environments. Berlin, Heidelberg: Springer; 2005.

[36] Buras R, Mayer B. Efficient unbiased variance reduction techniques for Monte Carlo simulations of radiative transfer in cloudy atmospheres: the solution. J Quant Spectrosc Radiat 2011;112(3):434–47. http://dx.doi.org/10.1016/j.jqsrt.2010.10.005.

[37] Mishchenko MI, Cairns B, Hansen JE, Travis LD, Burg R, Kaufman YJ, et al. Monitoring of aerosol forcing of climate from space: analysis of measurement requirements. J Quant Spectrosc Radiat 2004;88:149–61. http://dx.doi.org/10.1016/j.jqsrt.2004.03.030.

[38] Martin W, Cairns B, Bal G. Adjoint methods for adjusting three-dimensional atmosphere and surface properties to fit multi-angle/multi-pixel polarimetric measurements. J Quant Spectrosc Radiat 2014;144:68–85. http://dx.doi.org/10.1016/j.jqsrt.2014.03.030.